ACS APPLIED MATERIALS & INTERFACES

Research Article

www.acsami.org

Highly Porous Core–Shell Structured Graphene-Chitosan Beads

An Ouyang,[†] Chunhui Wang,[‡] Shiting Wu,[§] Enzheng Shi,[§] Wenqi Zhao,[‡] Anyuan Cao,*[,§] and Dehai Wu*[,†]

[†]Department of Mechanical Engineering, Tsinghua University, Beijing 100084, P. R. China

[‡]Center for Composite Materials and Structures, Harbin Institute of Technology, Harbin 150080, P.R. China

[§]Department of Materials Science and Engineering, College of Engineering, Peking University, Beijing 100871, P. R. China

Supporting Information

ABSTRACT: Graphene oxide (GO) sheets have been assembled into various three-dimensional porous structures and composites, with potential applications in energy and environmental areas. Here, we show the combination of GO and chitosan (CTS) into inorganic–organic heterocomposites as ∼3 mm diameter core–shell beads with controlled microstructure. The spherical GO-CTS beads, made by a two-step freeze-casting method, consist of a GO core wrapped by a CTS shell with abrupt interface; both parts have high porosities (94–96%) and mesopores volume (0.246 cm^3/g) yet with different pore morphologies. Incorporation of a GO core into the CTS beads significantly improved the methyl orange adsorption capacity (353 mg/g at 318 K) compared with pure CTS beads. Key factors such as the pH value, adsorbent dosage, concentration, time, and temperature have been studied in detail, whereas adsorption isotherm and kinetic studies reveal a Langmuir model following the pseudo-second order.

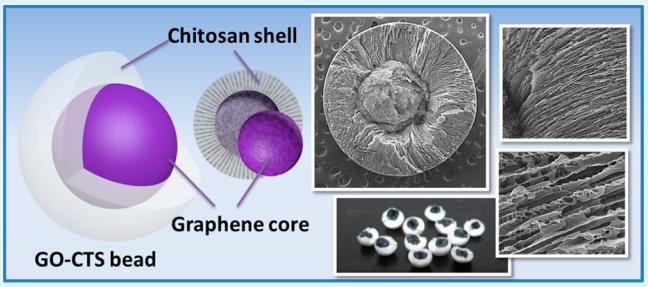

KEYWORDS: *graphene, chitosan, core–shell beads, freeze-casting, methyl orange adsorption*

1. INTRODUCTION

Graphene is a two-dimensional nanoscale building block that can be assembled into lightweight and highly porous bulk materials.[1−3] Various graphene-based aerogels, foams, networks, and fibers have been reported recently, with potential applications in energy and environmental fields as well as functional composites.[4−11] Integrating graphene, an inorganic nanostructure, with polymeric materials may enable hybrid composites and further extend their applications into more areas.[12−16] Chitosan, a biocompatible polymer derived from ocean plants, has found applications in adsorption, biosensing, and immobilization.[17−19] Graphene oxide sheets also have been mixed into CTS to make composite yarns and aerogels with improved mechanical strength and adsorption capacity.[20−24] In those composites, GO sheets as nanoscale fillers are uniformly distributed through the CTS matrix, resulting in a homogeneous pore morphology that generally appears as an interconnected three-dimensional (3D) network. Such uniform distribution and homogeneous microstructure are important factors for mechanical reinforcement and improved performance.[25,26] In addition, most previous GO-based adsorbents are in the form of bulk monoliths (e.g., cylinders) rather than spherical shapes that have particular applications in flowing liquid.

Here, we fabricate GO-CTS composite beads, not by uniformly mixing those two, but to form a hierarchical configuration that maintains the distinct microstructure of each component. This is enabled by the fact that either GO or CTS can be manufactured into 3D porous structures by similar processes (e.g., freeze-casting). The challenge remains in how to arrange different material components (inorganic versus organic) into predefined hierarchical configurations and create new functionality. As demonstration, we present a core–shell GO-CTS bead containing a GO core and a CTS shell that are integrated seamlessly with abrupt interface. These small beads are very stable, containing two different porous structures stemming from the GO and CTS part, respectively. This unique inorganic–organic core–shell structure brings advantages that individual components can hardly achieve. On one hand, coating a CTS shell on GO changes surface wettability and facilitates adsorption application in water. On the other hand, the incorporation of a GO core into CTS significantly enhances the adsorption capacity to dye molecules dissolved in water. Finally, the adsorption mechanism of our core–shell beads has been discussed by thermal dynamic and kinetic studies.

2. RESULTS AND DISCUSSION

2.1. Composite Characterization. Our core–shell beads were fabricated by a two-step freeze-casting process, in which the graphene core and the CTS shell were casted separately, in sequence, as illustrated in Figure 1a (see Experimental Section

Received: April 18, 2015
Accepted: June 16, 2015
Published: June 16, 2015

DOI: 10.1021/acsami.5b03369
ACS Appl. Mater. Interfaces 2015, 7, 14439−14445

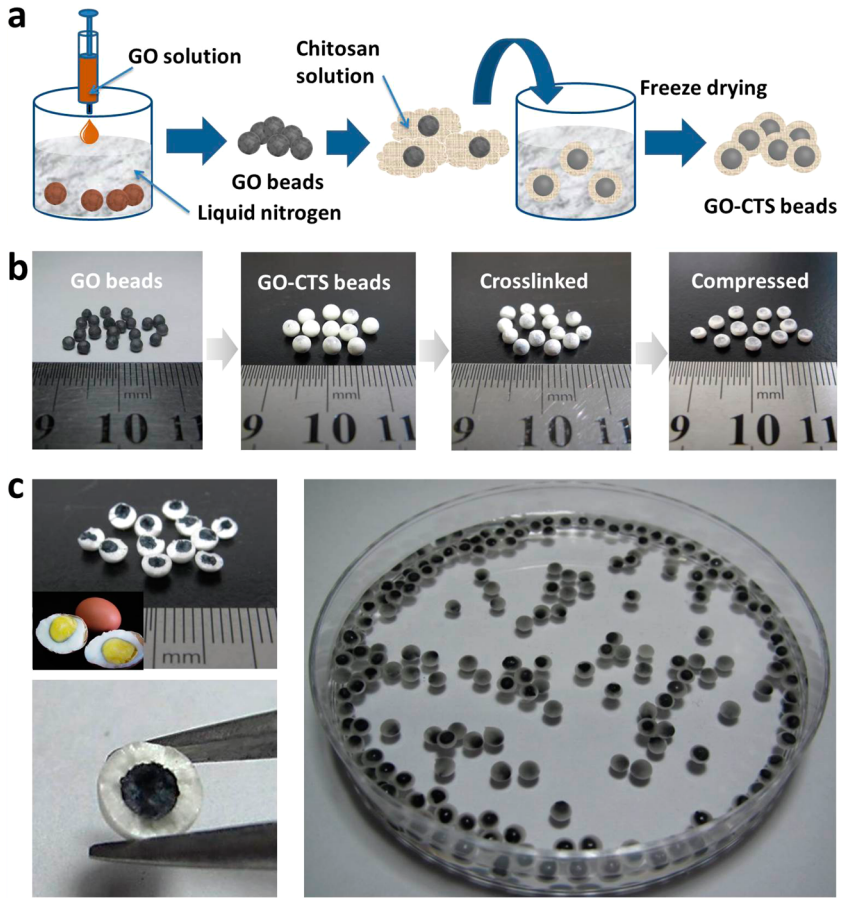

Figure 1. Fabrication of GO-CTS composite beads. (a) Illustration of the two-step freeze-casting process to make GO beads and GO-CTS beads in sequence. (b) Photos (from left to right) of GO beads, GO-CTS beads, cross-linked GO-CTS beads, and compressed GO-CTS beads. (c) Photos of half-cut GO-CTS beads and chicken eggs (inset) showing similar core−shell structure, and photo of GO-CTS beads immersed in water clearly revealing the GO core inside.

for details). Liquid nitrogen-assisted freeze-casting is a widely used method to manufacture various porous structures from biomaterials, polymers, and nanomaterials.[27−30] Here, porous GO beads were first made by dropping concentrated GO solution as small droplets into liquid nitrogen. These GO beads later became the core of the final core−shell structure, and also acted as the template to support the formation of the CTS shell in the second casting step. To make the CTS shell, a CTS solution was pasted around the GO beads, which was immersed in liquid nitrogen again for casting. Chemical reduction of GO beads was performed to render the bead surface hydrophobic and avoid infiltration of CTS into the GO pores. From Fourier transform infrared spectroscopy (FITR) analysis, the peak corresponding to C═O stretching (1716 cm^{-1}) has disappeared after reduction, indicating that graphene oxide has been completely reduced into rGO (Supporting Information, Figure S1). Therefore, the CTS shell only covers on the GO surface without entering the inside of the GO core. In addition to the GO-CTS beads, a reversed structure (the CTS-GO beads) can be fabricated by reversing the casting sequence (Figure S2 in the Supporting Information). In principle, higher level structures consisting of multiple GO and CTS layers are also possible with this method.

Digital photos recorded during the fabrication process clearly show the controllable structure evolution in each step (Figure 1b). As-synthesized GO beads (after hydrazine hydrate reduction) have a spherical shape with diameters of 1.5−2 mm. After coating the CTS shell, the beads grow larger (3−3.5 mm in diameter, porosities of 94% ∼ 96%, and 0.246 cm^3/g for mesopore volume) and appear white color. The dark GO core can still be seen through the outer shell. Cross-linking of the CTS shell was performed to avoid detachment of CTS during subsequent adsorption tests. The resulting core−shell beads, which are highly porous, can be compressed into a cakelike shape with a concave surface, indicating that the inner GO core is softer than the CTS shell.

Cross-sections of the broken beads show the core−shell structure in which a black core is surrounded by a white shell (Figure 1c). This structure is in analogous to chicken eggs consisting of egg york and white. Although bead samples with the GO core locating at the center of the bead have been obtained frequently, the manual pasting of CTS solution needs be improved to ensure a uniform coverage of CTS around the GO cores. These GO-CTS beads are rather stable in water; as the CTS shell adsorbs water and changes to a semitransparent hydrogel, the inside GO core with black color can be observed (Figure 1c, right-most picture).

Scanning electron microscopy (SEM) characterization clearly reveals the core−shell configuration of these GO-CTS beads, as illustrated in Figure 2a. Openings with short-range orientation appear on the bead surface; these are traces of negative replicas coming from dendritic ice crystals formed when the precursor droplets were immersed in liquid nitrogen (Figure 2b). In the cross-sectional view of a bead (in which part of the CTS shell

DOI: 10.1021/acsami.5b03369
ACS Appl. Mater. Interfaces 2015, 7, 14439−14445

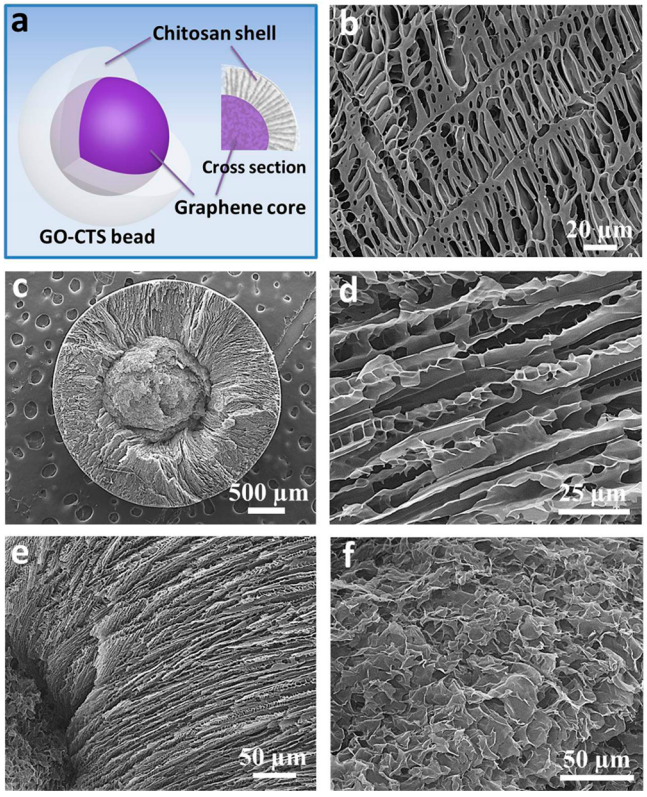

Figure 2. Structural characterization of the GO-CTS beads. (a) Illustration of the 3D core−shell structure. (b) SEM image of the surface morphology in a GO-CTS bead. (c) Cross-section of a bead showing a GO core embedded in the CTS shell. (d) SEM image of the CTS shell showing parallel and uniform channels. (e) View of the region between the GO core and CTS shell. (f) View of the GO core showing enclosed pores.

has been removed), one can see the exposed graphene core which is well-situated in the middle of the sphere (Figure 2c). The diameter of graphene core is 1.2 mm, whereas the CTS shell is about 0.6−0.8 mm thick. This leads to a core-to-shell volume ratio of about 1:7, and a graphene loading (weight percentage) of 3% in the entire bead. Close views of different parts across the cross-section also reveal distinct morphologies. In the CTS shell, there are long parallel channels extending from the core surface to the external surface of the bead (Figure 2d, e). These channels are the places where ice crystals grew and sublimed during the freeze-casting process. The widths of channels are in the range of 10−15 μm, indicating previous formation of uniform size ice crystals. In contrast, the inner core shows a very different morphology in which only random pores enclosed by GO sheets are present (Figure 2f). During freeze-casting of the GO core, ice crystals cannot grow into long straight channels (as in CTS) but rather form nearly enclosed cells, resulting in an isotropic morphology. The results also imply that GO sheets, being more rigid than polymer chains, can disturb or block the continuous growth of ice crystals. As a result, we obtain a hierarchical structure consisting of an organic shell (with parallel channels) and an inorganic core (with random cells); both are highly porous yet with different pore morphologies.

We also fabricated composites beads with CTS of different molar masses and concentrations in acid solutions, and characterized the pore morphology under these conditions. At the same CTS concentration (3 wt %), a lower molar mass (100 kDa) resulted in relatively larger channel sizes and thinner pore walls (Figure S3 in the Supporting Information). When the CTS concentration was reduced to 1.5 wt %, the inner and surface channel sizes increased further (up to 50 μm) (Figure S4 in the Supporting Information). These results indicate that the molar mass and concentration of CTS are two factors that can tailor the pore size.

In our two-step freeze-casting process, the GO core and CTS shell were formed separately, yet the core and shell adhere to each other very well (Figure 3a). Although with entirely

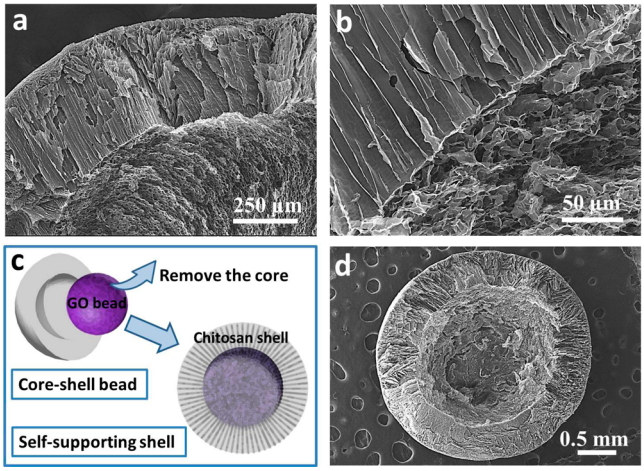

Figure 3. Characterization on the GO-CTS interface. (a) SEM image of the cross-section of a GO-CTS bead. (b) Close view of the interface showing aligned CTS channels terminate at the GO core. (c) Illustration on removal the GO core from the composite bead. (d) SEM image of the self-supporting CTS shell after GO removal.

different pore morphologies, the CTS shell and GO core have a sharp interface; one can see that those parallel CTS channels have terminated at the surface of the GO core (Figure 3b). One might imagine that when the CTS-pasted GO droplets were immersed in liquid nitrogen, straight needles of ice crystals started to grow inward and penetrate through the CTS shell until they arrived the GO core. Termination of ice growth is due to that the GO core contains virtually no water at the second freeze-casting step, as well as the higher resistance of GO sheets against ice crystal penetration; both factors result in the abrupt interface here. In addition, it is possible to remove the entire GO core from the bead without disturbing the aligned channels in the CTS layer (Figure 3c). This results in a clean, self-supporting, spherical CTS shell (Figure 3d). Thermogravimetric analysis (TGA) was taken to measure the thermal stability of the CTS and GO-CTS beads in air atmosphere (Figure S5a in the Supporting Information). The CTS beads have a steep mass loss at 250 °C with no residue, whereas the pure GO beads burns at temperature of 550−600 °C. In comparison, the GO-CTS beads show two consecutive mass decrease stages including a temperature region of ∼250−350 °C (burning of the outer CTS shell) and ∼350−600 °C (burning of the GO core), respectively. The introduction of GO inside CTS increases the thermal stability of the core−shell beads with reduced combustion rate.

To analyze the chemical structure in detail, we performed X-ray photoelectron spectroscopy (XPS) on the CTS shell, the GO and reduced GO (rGO) core (Figure S6 and Table S1 in the Supporting Information). The XPS results show the

DOI: 10.1021/acsami.5b03369
ACS Appl. Mater. Interfaces 2015, 7, 14439−14445

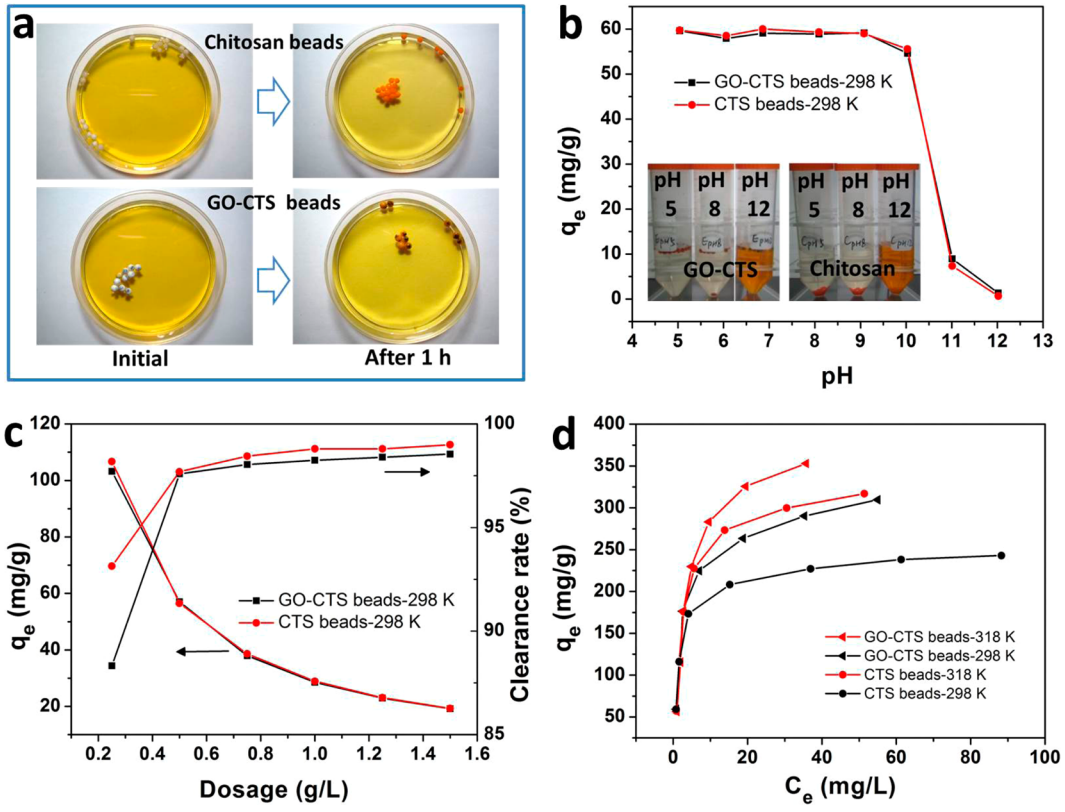

Figure 4. Adsorption tests. (a) CTS and GO-CTS beads placed in MO solutions at initial stage and after 1 h adsorption, and the beads have turned to yellow color. (b) Adsorption capacity at equilibrium (q_e) versus MO solution pH values for CTS and GO-CTS beads, respectively (original MO concentration is 30 mg/L). Inset, photos of MO solutions after adsorption at different pH conditions. (c) The q_e (left coordinate) and clearance rate (right coordinate) versus adsorbent dosage for CTS and GO-CTS beads, respectively (original MO concentration is 30 mg/L). (d) Equilibrium isotherms for CTS and GO-CTS beads at 298 and 318 K, respectively.

existence of C 1s, N 1s and O 1s peaks in both the core and shell parts. The oxygen-containing species of C−O (carbon in epoxy group), C═O (carbon in carbonyl group) and COOH (carbon in carboxylic acid) decrease significantly, indicating the removal of oxygen during reduction (from GO to rGO). In the CTS shell, the N 1s content is much higher than that in the rGO core. Fourier Transform Infrared Spectroscopy (FTIR) of the CTS shell also show CTS-related peaks, including the C−O stretching vibrations (1065 cm^{-1}), C−H stretching vibrations (2872 cm^{-1}) and N−H bending of primary amine (1556, 1629 cm^{-1}). Stretching peaks of saturated deformation vibration C−H (1379 cm^{-1}) appear in both the CTS shell and the GO core (Figure S1 in the Supporting Information).

2.2. Sorption Results. To remove dye molecules from solutions, methods such as adsorption by porous GO and polymeric materials have been extensively studied.[31−33] The presence of CTS shells enables adsorption application in aqueous environment. When the core−shell beads and pure CTS beads (control sample) were placed in a methyl orange (MO) solution, those beads quickly became wetting to water, and sank into the solution. Efficient MO adsorption could be observed from the concentrated yellow color on both types of beads, and the weakening of solution color after a certain period (Figure 4a). We find that a suitable environment for adsorption is from acidic to weak alkaline (with adsorption capacities of nearly 60 mg/g in a pH range of 5.04 to 9.08), while in strong alkaline condition (pH up to 12.02) the capacities dropped substantially (Figure 4b). The adsorption capacity is defined as the removed MO mass relative to the mass of total beads in the solution, determined by the initial and final MO concentrations which can be calculated by the change of optical absorption intensity at 465 nm (characteristic band of MO) during tests. Meanwhile, at this relatively low MO concentration (30 mg/L), the CTS and GO-CTS beads show almost the same adsorption capacities, indicating that at this stage it is the porous CTS (shell) being responsible for molecular adsorption.

Certainly, the adsorption capacity depends on how much beads have been placed in the solution (dosage). In general, the adsorption capacity of GO-CTS beads to MO (at equilibrium) decreases monotonically as the dosage increases; significant capacity loss (from 103 down to 19 mg/g) accompanies a 6-fold increase of dosage (from 0.25 to 1.5 g/L) (Figure 4c). Meanwhile, the removal percentage of GO-CTS beads for MO (adsorbed versus original amount) increases from 88% at a dosage of 0.25 g/L to nearly 98% at higher dosages. Although a higher dosage means more available adsorption sites provided by the beads, the removal percentage finally stabilizes as most of the MO molecules have been adsorbed.

Although their adsorption capacities are quite similar at low initial MO concentration (30 mg/L), the CTS and GO-CTS beads show some different behavior at high concentration environment. For MO solutions with initial concentrations (C_0) of 30 to 210 mg/L and a fixed dosage of 0.5 g/L put in each solution, we have measured the equilibrium concentration (C_e) and the adsorption capacity (q_e) after the solutions reached equilibrium (Figure 4d). At the same C_0 in this range, the GO-CTS beads exhibit higher q_e and correspondingly lower

DOI: 10.1021/acsami.5b03369
ACS Appl. Mater. Interfaces 2015, 7, 14439−14445

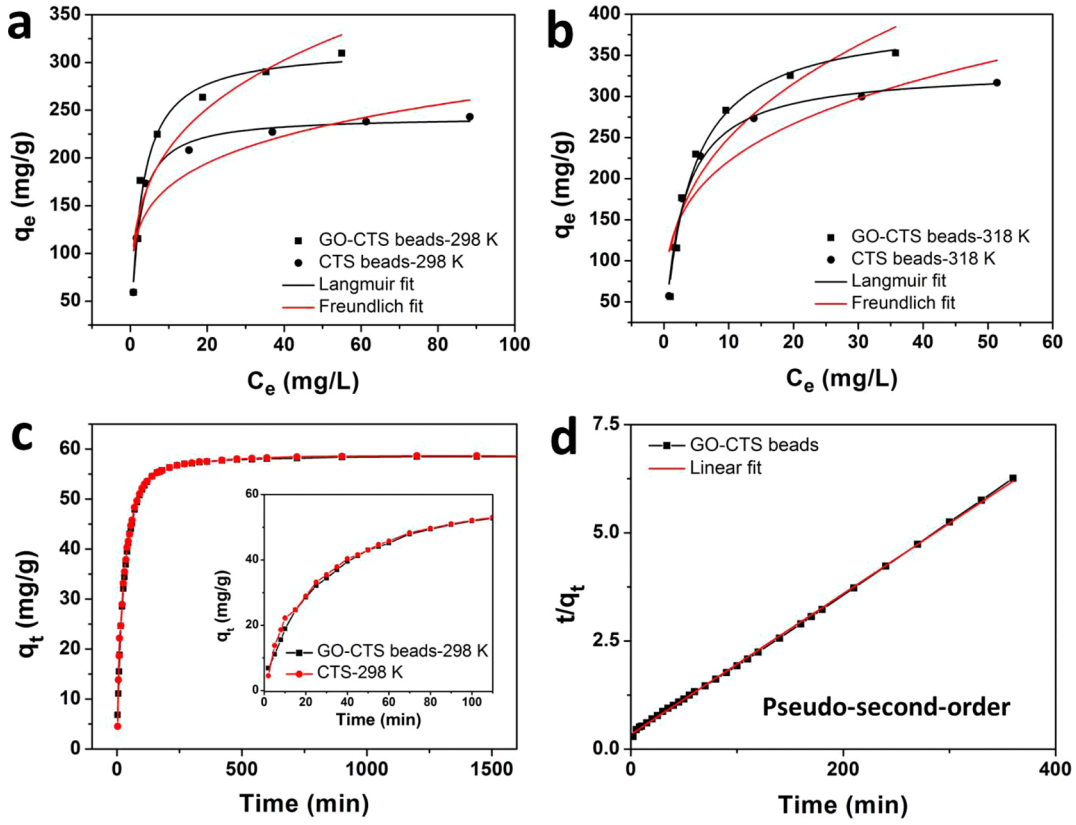

Figure 5. Adsorption isotherms and kinetics of GO-CTS and CTS beads. Langmuir and Freundlich fitting of adsorption isotherms by GO-CTS and CTS beads, respectively, at temperatures of (a) 298 K and (b) 318 K. (c) Adsorption capacity recorded during an adsorption period of 1500 min. Inset, enlarged view of the beginning stage. (d) Pseudo-second order linear fitting of the curve (t/q_t versus adsorption time) by the GO-CTS beads.

C_e than that of the CTS beads, and this difference becomes larger with increasing C_0 up to 210 mg/L. Furthermore, when the temperature increases from 298 to 318 K, the adsorption capacity also enhances and the equilibrium concentration further decreases (Figure 4d). This indicates that the MO adsorption on CTS surface is an endothermic process. At those temperatures, the GO-CTS beads have higher q_e (reaching 353 mg/g at 318 K) than CTS beads (317 mg/g); we think their structural difference plays an important role here. First, incorporation of a GO core has enlarged the specific surface area of CTS beads (from about 5.1 to 26.7 m^2/g) with negligible additional weight (<3%) (Figure S5b in the Supporting Information). Second, at lower MO concentration (30 mg/L-60 mg/L), CTS dominates the adsorption process therefore both CTS and core−shell beads have similar performance (Figure 4b, 4c). Whereas at higher MO concentration (90−210 mg/L), the GO core starts to play effect by providing more adsorption sites. From SEM images, the inside GO core may be accessible to liquid molecules transported through the porous channels in the CTS shell and enhance molecular adsorption. A summary of reported MO adsorption capacities using various adsorbents is shown in Table S2 in the Supporting Information. It is rather difficult to directly compare the results due to different initial MO concentrations. However, it can be seen that our GO-CTS beads have relatively higher adsorption capacity at similar initial MO concentrations among various composite materials containing carbon nanotubes or GO. The adsorption capacity might be further improved by tailoring the structure of GO core and CTS shell.

2.3. Adsorption Isotherm and Kinetics. We have used the Langmuir model to fit and analyze the adsorption isotherm data presented in Figure 4d, by the following equation: $(C_e/q_e) = (C_e/q_{max}) + (1q_{max}K_L)$, where q_{max} is the maximum adsorption capacity and K_L is the Langmuir constant representing the affinity between the adsorbent and adsorbate. This yielded correlation coefficients (R^2) of 0.9864 and 0.9707 for the adsorption isotherm (at 298 K) of CTS beads and core−shell beads, respectively (Figure 5a). The value of q_{max} (~316 mg/g) derived from the Langmuir equation is very close to experimental measurement (~310 mg/g). At the same time, we also fitted the data by the Freundlich model, which generated lower coefficients (R^2 =0.8417 and 0.8729 for CTS and core−shell, respectively) (Table S3 in the Supporting Information). Furthermore, the adsorption isotherm at higher temperature (318 K) also can be well-fitted by the Langmuir model (Figure 5b, Table S4 in the Supporting Information). The above results indicate that the monolayer MO adsorption takes place on homogeneously distributed active sites among the CTS channels by equivalent sorption energies, according to the Langmuir model.[34,35]

We also studied the adsorption kinetics by measuring the instantaneous adsorption capacity during the adsorption process at an initial MO concentration of 30 mg/L, in which the CTS and core−shell beads displayed similar behavior. At the beginning (within 20 min), the process was fast with an adsorption rate of 1.42 and 1.38 mg/(g min) for CTS and core−shell beads, which then saturated until equilibrium (Figure 5c). The adsorption rates over time can be well fitted by the pseudo-second-order model, yielding correlation

DOI: 10.1021/acsami.5b03369
ACS Appl. Mater. Interfaces 2015, 7, 14439−14445

coefficients of R^2 = 0.9996 and 0.9995 for CTS and core−shell beads, respectively, compared with the pseudo-first-order and the Elovich models (Figure 5d). Also, the calculated equilibrium adsorption capacities fit well with the experimental data (Table S5 and Figure S7 in the Supporting Information). The results indicate that the overall rate of adsorption process appears to be controlled by the chemical process, which may involve valency forces through sharing or exchange of electrons between dye anions and adsorbent.[36,37]

3. CONCLUSION

We demonstrated controlled fabrication of graphene oxide and CTS composite beads with a unique core−shell structure integrating different pore morphologies. These composite beads show enhanced molecular adsorption in water solution, owing to the incorporation of a graphene core within the CTS shell. Our method might be used to synthesize hierarchical porous structures consisting of multiple inorganic and organic layers with sharp interface and tunable layer thickness. Despite their entirely different material properties and pore structures, GO and CTS can be integrated into stable, hierarchical configurations with extended applications than individual components. Our highly porous graphene/chitosan beads have potential applications in energy, environmental, and biomedical areas.

4. EXPERIMENTAL SECTION

4.1. Materials. Graphene oxide sheets dispersed in water were synthesized via the Hummers' method.[38] Chitosan with a higher molar mass of ∼620 kDa (B.R. Sinopharm Chemical Reagent Co., Ltd.) had deacetylation degree between 80% ∼ 90%, and chitosan with a lower molar mass of ∼100 kDa (Zhejiang Golden-shell pharmaceutical Co., Ltd.) had deacetylation degree of 80%. Glacial acetic acid (A.R. Beijing Chemical Works) was used to dissolve the chitosan powders and epichlorohydrin (Beijing Yili Fine Chemicals Co., Ltd.) was used as the cross-linking agent. Liquid nitrogen (−196 °C, degree of purity) was cooling medium for freeze casting.

4.2. Synthesis of Graphene and Chitosan Composite Beads. The GO-CTS beads were fabricated by a two-step freeze-casting process. In the first step, an aqueous solution GO sheets with a concentration of (about 8 mg/mL) was injected through a syringe needle (0.7 mm in diameter) into liquid nitrogen (−196 °C) as small droplets (1.5−2 mm in diameter), then the frozen GO-water droplets were collected and freeze-dried to make porous GO cores. These GO beads were reduced chemically by hydrazine vapor at 90 °C for 24 h. In the second step, the chitosan powders were dissolved in 2% acetic acid solution, following by magnetic stirring for 1 h. Then, the reduced GO beads were wrapped by a CTS solution (3 or 1.5 wt %) uniformly and placed into liquid nitrogen again to freeze the CTS shell. Dry and porous GO-CTS beads were formed after freeze-drying and the thickness of CTS shell could be changed by the CTS solution concentrations. The GO-CTS beads were immersed in epichlorohydrin solution for cross-linking, heating in 50 °C water bath for 5 h. The reversed structure (CTS wrapped by GO) and the control sample (bare CTS beads) were fabricated using the same method.

4.3. Sample Characterization. SEM characterization was performed on LEO-1530 field emission electron microscope. The surface area and pore size distribution of GO-CTS and CTS beads were analyzed by the Brunner−Emmet−Teller (BET) method and Barrett−Joyner−Halen (BJH) method respectively using nitrogen adsorption−desorption isotherm at 77 k on NOVA4000. TGA analysis was carried out on TGA 2050 at temperature range from 30 to 800 °C in air. XPS spectra were obtained using PHI Quantera SXM and FTIR spectra were obtained using Nicolet 6700 FTIR. The XPS spectra were calibrated to the C−C peak at 284.8 eV. UV−vis spectra were carried out by Cary 5000 (Agilent Company) to determine the concentrations of MO solutions.

4.4. Adsorption of Methyl Orange. Adsorption of MO was conducted by adding certain adsorbents (GO-CTS and CTS beads) into aqueous solution, and shaking the solution until the equilibrium state. We studied the influence of pH on MO adsorption by varying the solution pH from 5.04 to 12.02 adjusted by HAc or NaOH solution, in C_0 of 30 mg/L and a fixed dosage of 0.5 g/L, 298 K. Test on the dosage (0.25−1.5 g/L) of adsorbents in MO solution was conducted at neutral solution in C_0 of 30 mg/L, 298 K. The adsorption isotherm were studied in different C_0 of 30−210 mg/L at both 298 and 318 K, and the adsorption kinetics were studied in C_0 of 30 mg/L and a fixed dosage of 0.5 g/L, 298 K. The concentration of MO was analyzed based on the optical absorption intensity at 465 nm recorded by Cary 5000 after certain adsorption period or at equilibrium. Then, the adsorption capacity can be calculated as follows

$$q_t = \left(\frac{V(C_0 - C_t)}{m}\right) \text{mg/g} \quad (1)$$

$$q_e = \left(\frac{V(C_0 - C_e)}{m}\right) \text{mg/g} \quad (2)$$

$$C\% = \frac{(C_0 - C_e)}{C_0} 100\% \quad (3)$$

Where C_t (mg/L) is the concentration at predetermined time t, V (mL) is the total volume of the aqueous solution, and m (mg) is the weight of the adsorbent. The q_t (mg/g) and q_e (mg/g) is the MO adsorption capacity at time t and equilibrium, respectively. $C\%$ is the clearance rate.

■ ASSOCIATED CONTENT

Ⓢ Supporting Information

SEM characterization of reversed bead structure; beads prepared from CTS with different molar masses and concentrations; XPS, FTIR, TGA, and BET results; summary of MO adsorption from literature; adsorption isotherms and kinetics analysis. The Supporting Information is available free of charge on the ACS Publications website at DOI: 10.1021/acsami.5b03369.

■ AUTHOR INFORMATION

Corresponding Authors

*E-mail: anyuan@pku.edu.cn.
*E-mail: wdh_thu@foxmail.com.

Notes

The authors declare no competing financial interest.

■ ACKNOWLEDGMENTS

A.C. acknowledges the National Natural Science Foundation of China (NSFC) under the Grant 51325202.

■ REFERENCES

(1) Geim, A. K. Graphene: Status and Prospects. *Science* **2009**, *324*, 1530−1534.
(2) Jiang, H.; Lee, P. S.; Li, C. 3D Carbon Based Nanostructures for Advanced Supercapacitors. *Energy Environ. Sci.* **2013**, *6*, 41−53.
(3) Worsley, M. A.; Pauzauskie, P. J.; Olson, T. Y.; Biener, J.; Satcher, J. H., Jr; Baumann, T. F. Synthesis of Graphene Aerogel with High Electrical Conductivity. *J. Am. Chem. Soc.* **2010**, *132*, 14067−14069.
(4) Compton, O. C.; Nguyen, S. T. Graphene Oxide, Highly Reduced Graphene Oxide, and Graphene: Versatile Building Blocks for Carbon-Based Materials. *Small* **2010**, *6*, 711−723.
(5) Sudeep, P. M.; Narayanan, T. N.; Ganesan, A.; Shaijumon, M. M.; Yang, H.; Ozden, S.; Patra, P. K.; Pasquali, M.; Vajtai, R.; Ganguli, S.

DOI: 10.1021/acsami.5b03369
ACS Appl. Mater. Interfaces 2015, 7, 14439−14445

Covalently Interconnected Three-Dimensional Graphene Oxide Solids. *ACS Nano* **2013**, *7*, 7034−7040.
(6) Li, Y.; Chen, J.; Huang, L.; Li, C.; Hong, J. D.; Shi, G. Highly Compressible Macroporous Graphene Monoliths Via an Improved Hydrothermal Process. *Adv. Mater.* **2014**, *26*, 4789−4793.
(7) Zhao, J.; Ren, W.; Cheng, H. Graphene Sponge for Efficient and Repeatable Adsorption and Desorption of Water Contaminations. *J. Mater. Chem.* **2012**, *22*, 20197−20202.
(8) Liu, Z.; Li, Z.; Xu, Z.; Xia, Z.; Hu, X.; Kou, L.; Peng, L.; Wei, Y.; Gao, C. Wet-Spun Continuous Graphene Films. *Chem. Mater.* **2014**, *26*, 6786−6795.
(9) Hu, H.; Zhao, Z.; Wan, W.; Gogotsi, Y.; Qiu, J. Ultralight and Highly Compressible Graphene Aerogels. *Adv. Mater.* **2013**, *25*, 2219−2223.
(10) Xu, Z.; Zhang, Y.; Li, P.; Gao, C. Strong, Conductive, Lightweight, Neat Graphene Aerogel Fibers with Aligned Pores. *ACS Nano* **2012**, *6*, 7103−7113.
(11) Yao, H. B.; Ge, J.; Wang, C. F.; Wang, X.; Hu, W.; Zheng, Z. J.; Ni, Y.; Yu, S. H. A Flexibleand Highly Pressure-Sensitive Graphene-Polyurethane Sponge Based On Fractured Microstructure Design. *Adv. Mater.* **2013**, *25*, 6692−6698.
(12) Singh, V.; Joung, D.; Zhai, L.; Das, S.; Khondaker, S. I.; Seal, S. Graphene Based Materials: Past, Present and Future. *Prog. Mater. Sci.* **2011**, *56*, 1178−1271.
(13) Niu, Z.; Liu, L.; Zhang, L.; Shao, Q.; Zhou, W.; Chen, X.; Xie, S. A Universal Strategy to Prepare Functional Porous Graphene Hybrid Architectures. *Adv. Mater.* **2014**, *26*, 3681−3687.
(14) Wang, N.; Chang, P. R.; Zheng, P.; Ma, X. Graphene-Poly (Vinyl Alcohol) Composites: Fabrication, Adsorption and Electrochemical Properties. *Appl. Surf. Sci.* **2014**, *314*, 815−821.
(15) Vickery, J. L.; Patil, A. J.; Mann, S. Fabrication of Graphene-Polymer Nanocomposites with Higher-Order Three-Dimensional Architectures. *Adv. Mater.* **2009**, *21*, 2180−2184.
(16) Xu, Y.; Hong, W.; Bai, H.; Li, C.; Shi, G. Strong and Ductile Poly (Vinyl Alcohol)/Graphene Oxide Composite Films with a Layered Structure. *Carbon* **2009**, *47*, 3538−3543.
(17) Kumar, M. N. R. A Review of Chitin and Chitosan Applications. *React. Funct. Polym.* **2000**, *46*, 1−27.
(18) Kim, J.; Kim, Y.; Park, K.; Kang, E.; Lee, S.; Nam, H. Y.; Kim, K.; Park, J. H.; Chi, D. Y.; Park, R. Self-Assembled Glycol Chitosan Nanoparticles for the Sustained and Prolonged Delivery of Antiangiogenic Small Peptide Drugs in Cancer Therapy. *Biomaterials* **2008**, *29*, 1920−1930.
(19) Kim, I.; Seo, S.; Moon, H.; Yoo, M.; Park, I.; Kim, B.; Cho, C.; Chi, D. Y.; Park, R. Chitosan and its Derivatives for Tissue Engineering Applications. *Biotechnol. Adv.* **2008**, *26*, 1−21.
(20) Bao, H.; Pan, Y.; Ping, Y.; Sahoo, N. G.; Wu, T.; Li, L.; Li, J.; Gan, L. H.; Park, R. Chitosan-Functionalized Graphene Oxide as a Nanocarrier for Drug and Gene Delivery. *Small* **2011**, *7*, 1569−1578.
(21) Li, Y.; Sun, J.; Du, Q.; Zhang, L.; Yang, X.; Wu, S.; Xia, Y.; Wang, Z.; Xia, L.; Cao, A. Mechanical and Dye Adsorption Properties of Graphene Oxide/Chitosan Composite Fibers Prepared by Wet Spinning. *Carbohyd. Polym.* **2014**, *102*, 755−761.
(22) Shi, H.; Li, W.; Zhong, L.; Xu, C. Methylene Blue Adsorption from Aqueous Solution by Magnetic Cellulose/Graphene Oxide Composite: Equilibrium, Kinetics, and Thermodynamics. *Ind. Eng. Chem. Res.* **2014**, *53*, 1108−1118.
(23) Yang, X.; Tu, Y.; Li, L.; Shang, S.; Tao, X. Well-Dispersed Chitosan/Graphene Oxide Nanocomposites. *ACS Appl. Mater. Interfaces* **2010**, *2*, 1707−1713.
(24) He, Y. Q.; Zhang, N. N.; Wang, X. D. Adsorption of Graphene Oxide/Chitosan Porous Materials for Metal Ions. *Chin. Chem. Lett.* **2011**, *22*, 859−862.
(25) Fan, H.; Wang, L.; Zhao, K.; Li, N.; Shi, Z.; Ge, Z.; Jin, Z. Fabrication, Mechanical Properties, and Biocompatibility of Graphene-Reinforced Chitosan Composites. *Biomacromolecules* **2010**, *11*, 2345−2351.
(26) Pan, Y.; Wu, T.; Bao, H.; Li, L. Green Fabrication of Chitosan Films Reinforced with Parallel Aligned Graphene Oxide. *Carbohyd. Polym.* **2011**, *83*, 1908−1915.
(27) Deville, S.; Saiz, E.; Nalla, R. K.; Tomsia, A. P. Freezing as a Path to Build Complex Composites. *Science* **2006**, *311*, 515−518.
(28) Ouyang, A.; Liang, J. Tailoring the Adsorption Rate of Porous Chitosan and Chitosan Carbon Nanotube Core-Shell Beads. *RSC Adv.* **2014**, *4*, 25835−25842.
(29) Klotz, M.; Amirouche, I.; Guizard, C.; Viazzi, C.; Deville, S. Ice Templating-an Alternative Technology to Produce Micromonoliths. *Adv. Eng. Mater.* **2012**, *14*, 1123−1127.
(30) Ouyang, A.; Gong, Q.; Liang, J. Carbon Nanotube−Chitosan Composite Beads with Radially Aligned Channels and Nanotube-Exposed Walls for Bilirubin Adsorption. *Adv. Eng. Mater.* **2015**, *17*, 460−466.
(31) Wang, Y.; Xia, G.; Wu, C.; Sun, J.; Song, R.; Huang, W. Porous Chitosan Doped with Graphene Oxide as Highly Effective Adsorbent for Methyl Orange and Amido Black 10B. *Carbohyd. Polym.* **2015**, *115*, 686−693.
(32) Dragan, E. S.; Loghin, D. F. A. Enhanced Sorption of Methylene Blue From Aqueous Solutions by semi-IPN Composite Cryogels with Anionically Modified Potato Starch Entrapped in PAAm. Matrix. *Chem. Eng. J.* **2013**, *234*, 211−222.
(33) Fan, L.; Luo, C.; Sun, M.; Qiu, H.; Li, X. Synthesis of Magnetic β-Cyclodextrin−Chitosan/Graphene Oxide as Nanoadsorbent and its Application in Dye Adsorption and Removal. *Colloids Surf. B* **2013**, *103*, 601−607.
(34) Langmuir, I. The Adsorption of Gases On Plane Surfaces of Glass, Mica and Platinum. *J. Am. Chem. Soc.* **1918**, *40*, 1361−1403.
(35) Freundlich, H. Adsorption in Solutions. *Z. Phys. Chem.* **1906**, *57*, 384−470.
(36) Ho, Y.; McKay, G. Pseudo-Second Order Model for Sorption Processes. *Process Biochem.* **1999**, *34*, 451−465.
(37) Ho, Y.; McKay, G. The Kinetics of Sorption of Divalent Metal Ions Onto Sphagnum Moss Peat. *Water Res.* **2000**, *34*, 735−742.
(38) Hummers, W. S., Jr; Offeman, R. E. Preparation of Graphitic Oxide. *J. Am. Chem. Soc.* **1958**, *80*, 1339−1339.

DOI: 10.1021/acsami.5b03369
ACS Appl. Mater. Interfaces 2015, 7, 14439−14445